Determining the Magnetic Field Strength in OMC-1: Analyzing Angular Dispersion Calculation Methods

Arianna Imperiali

November 30, 2021

ABSTRACT

Studying magnetic fields across the Galaxy has become an essential part of understanding star formation and the role that magnetic support plays in gravitational cloud collapse. Recently, two distinguished groups, Chuss et al. (2019) and Hwang et al. (2021), have published separate works calculating the magnetic field strength for a region in our Galaxy, the Orion Molecular Cloud 1 (OMC-1). In each of these works, the Davis-Chandrasekhar-Fermi (DCF) method was employed to create maps of volume density, velocity dispersion, and angular dispersion to ultimately calculate the magnetic field strength of the region. Chuss et al. (2019) found magnetic field strengths ranging from a few hundred μG to up to 2000 μG. Hwang et al. (2021) found magnetic field strengths that vary from 800 to 24600 μG. This paper analyzes the methods used by each group in calculating the angular dispersion component of the DCF method to gauge whether or not it made a contribution to the large variation in magnetic field strength calculations. It was found that the angular dispersion within OMC-1 calculated by Chuss et al. (2019) and Hwang et al. (2021) was quite different; therefore, we can conclude that the different methods used to calculate this component did have a significant effect on the resulting magnetic field strength calculations. This analysis provides invaluable input into gauging the reasons for the differences in results and will establish discussions about the accuracy of methods in calculating angular dispersions.

1 Introduction

1.1 Mapping Magnetic Fields

Far-Infrared (FIR) dust polarimetry has provided astronomers with new methods to study and map the distribution of magnetic fields in the diffuse Interstellar Medium (ISM) and molecular clouds throughout the Galaxy. Through a method known as radiative alignment torque, starlight can transfer angular momentum to dust grains, causing them to align their longest axes perpendicular to magnetic fields. This results in an observed polarization direction perpendicular to the magnetic field direction which is projected onto the plane of the sky (Lazarian & Hoang, 2007).

There are two primary components to magnetic fields in the universe. The first is the large-scale, ordered magnetic field, which is spatially coherent at the scale of the region being studied. The other is the small-scale magnetic field, which is caused by magnetic fluctuations, or turbulence, at different scales within the region (Schekochihin & Cowley, 2007). To determine total magnetic field strength distributions in molecular clouds, Chandrasekhar & Fermi (1953) created the Davis-Chandrasekhar-Fermi (DCF) method. The DCF method relates the velocity dispersion along the line-of-sight to the polarization angle dispersion on the plane-of-sky and assumes an isotropically turbulent medium,

whose turbulent and magnetic energy components are in equipartition (Heitsch, 2005). Hildebrand et al. (2009) and Houde et al. (2009) developed upon the DCF method to determine the dispersion of magnetic field vectors in molecular clouds due to turbulence. The distortion of magnetic field lines by turbulence is reflected into the dispersion of the polarization angles of the observed light reflected off the dust grains (Hildebrand et al., 2009). Hildebrand et al. (2009) and Houde et al. (2009) equate the kinetic energy from the turbulence to the dispersion of magnetic field polarization vectors, as seen through the dust grain alignment, to estimate the magnetic field strength. The magnetic field strength can be determined through means of the DCF method by utilizing Equation 1, which relates the magnetic field strength, B, to the volume density of the gas in the cloud, ρ, velocity dispersion of the gas coupled to the magnetic field, σ_v, and angular dispersion of magnetic field vectors, σ_ϕ (Chandrasekhar & Fermi, 1953):

$$B^2 = 4\pi\rho\frac{\sigma_v^2}{\sigma_\phi^2}. \tag{1}$$

The Orion Molecular Cloud (OMC) is the closest sight of massive star formation, ~ 390 pc away (Kounkel et al., 2017). Recently, two different groups, Chuss et al. (2019) and Hwang et al. (2021), obtained observations of a region in this cloud complex, OMC-1, which contains molecular gas and dust in the form of a ridge oriented roughly North-South (Guerra et al., 2021). On the West side of OMC-1, there is the BN object (a massive young stellar object) surrounded by the KL nebula (molecular gas and dust surrounding massive stars) (Becklin & Neugebauer, 1967; Kleinmann & Low, 1967) (to be referred to as the BNKL object throughout the rest of this paper). Southeast in the region is the Orion Bar, which bounds the HII region created by stars in the Trapezium Cluster and contains a photon-dominated region at the boundary between the HII region and molecular material (Chuss et al., 2019). The radiation emitted from these objects in OMC-1 affects dust grain alignment throughout the region (Lazarian & Hoang, 2007). Figure 1 depicts these three regions in OMC-1, as shown in Guerra et al. (2021).

The objective of using dust polarimetry to map magnetic fields in OMC-1 is to better understand the relationship between the star formation process and gravitational collapse. Magnetic turbulence in molecular clouds regulates star forming activity in the ISM (Guerra et al., 2021). Astronomers who have previously mapped OMC-1 (e.g. Schleuning, 1998; Vallee & Bastien, 1999; Houde et al., 2004; Ward-Thompson et al., 2017) have found that the magnetic field in OMC-1 exhibits a pinch in the orthogonal direction to make an hourglass shape, which has been interpreted to indicate that the star formation in the OMC-1 region is magnetically regulated. Across magnetic field lines, gravitational collapse compresses the field lines to create regions of enhanced field strength; however, gravitational collapse can also be slowed by magnetic pressure (Guerra et al., 2021). Therefore, gauging whether a cloud will collapse depends on the relationship between mass and magnetic flux in the region.

1.2 Comparison of Magnetic Field Strength Calculation Methods

Chuss et al. (2019) obtained photometry and polarimetry for the OMC-1 region using the High-resolution Airborne Wideband Camera (HAWC+) on board the Stratospheric Observatory for Infrared Astronomy (SOFIA) (Harper et al., 2018). Measurements were taken at four different wavelengths in the FIR of 53, 89, 154, and 214 μm. Chuss et al. (2019) combined these observations with photometry, also obtained by HAWC+, within millimeter regimes to produce Spectral Energy Distributions (SEDs). They utilized these data to develop distribution maps, over the entirety of OMC-1, corresponding to each of the components in Equation 1.

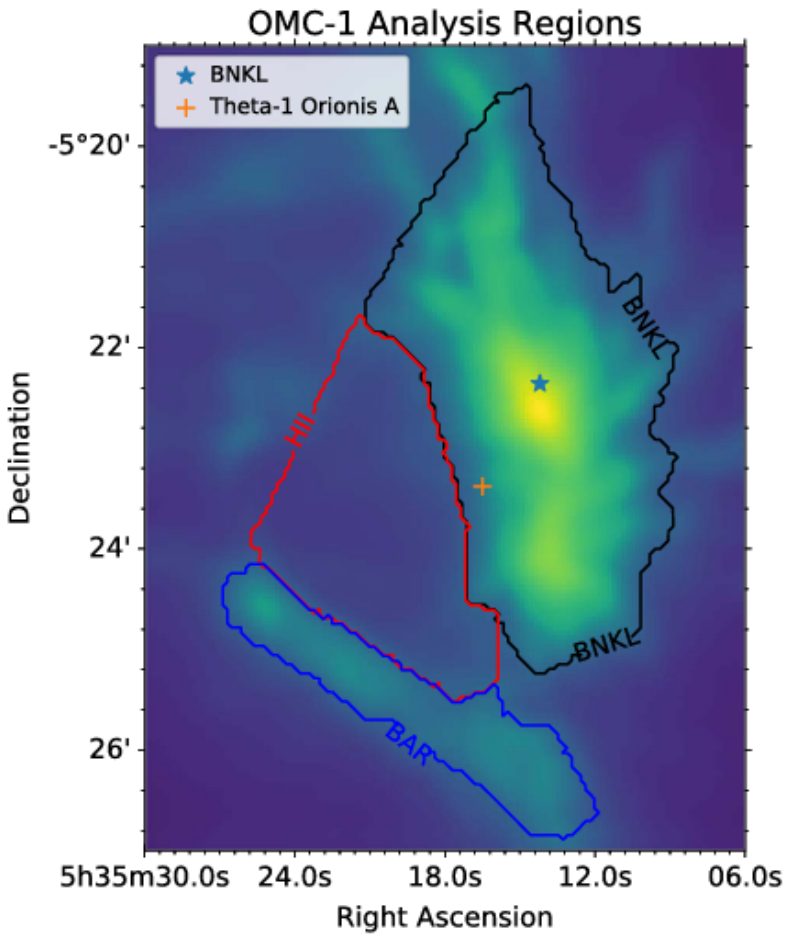

Figure 1: Three regions of OMC-1 are indicated by a black outline (BNKL), a red outline (HII region), and a blue outline (Orion Bar) Guerra et al. (2021).

They first obtained a volume density map of molecular hydrogen by fitting the SEDs of infrared emission from OMC-1 in the range of 53 μm to 35 mm. They created a velocity dispersion map through the emission line spectra of the molecular tracer NH_3. NH_3 has been used as a probe of dense clouds, and the particular emission line transition (1,1), as described in Friesen et al. (2017), is highly correlated with dust column density. See Chuss et al. (2019) for a discussion of details about the velocity dispersion and volume density calculation methods. In order to map the angular dispersion distribution, they applied a function to describe the dispersion of magnetic field vectors to the polarimetry data at each wavelength measurement at each pixel. See Chuss et al. (2019) and Guerra et al. (2021) for a discussion of details about this function and how it was employed. The maps of each component of Equation 1 were combined to produce maps of the magnetic field strength distribution along the plane-of-sky B at each wavelength. B values range from $\sim$100 μG to $\sim$ 2000 μG. The largest field strengths are consistently observed around and South of the BNKL object while weaker field strengths are observed in the Bar region.

Hwang et al. (2021) obtained polarimetry and total intensity observations of OMC-1 with the POL-2 polarimeter on the Submillimetre Common-User Bolometer Array 2 (SCUBA-2) camera at 450 and 850 μm (Friberg et al., 2016). This observation was a part of the James Clerk Maxwell Telescope (JCMT) program, B-fields in STar-forming Region Observations (BISTRO). They also

used the Heterodyne Array Receiver Program (HARP) spectrometer to obtain the profiles of the $C^{18}O$ spectral lines. Because the observations from Hwang et al. (2021) are not utilized in the methodology for this study, this is the extent to which they will be discussed. See Hwang et al. (2021) for additional details about the SCUBA-2 observations taken. Hwang et al. (2021) estimated the volume density of molecular hydrogen from the continuum observations at 450 and 850 μm. They used the $C^{18}O$ spectral line profiles from HARP to measure the velocity dispersion. To find the angular dispersion, they utilized a method, first developed by Pattle et al. (2017), analogous to the common image smoothing technique 'unsharp masking.' Since in molecular clouds there are two main components to the measured magnetic field dispersion, it is difficult to determine the local magnetic field dispersion directly from polarization observations (Hwang et al., 2021). Therefore, in order to measure the large-scale field geometry, Pattle et al. (2017) estimated the mean field orientation in a small moving 5" $\times$ 5" box throughout the image. By moving the box and estimating over the entire region, it was possible to trace the large-scale magnetic field, and consequently, create a map of the small scale, turbulent magnetic field component. Finally, they estimated the angular dispersion of magnetic field lines by calculating the root-mean-square of the angle differences in this resulting map. A more detailed description of the 'unsharp masking' technique is provided in Section 3 as it is performed in this study. Pattle et al. (2017) found good agreement between this moving box average and the true field direction using Monte Carlo simulations. The three components of the DCF method were then used to compose a map of the magnetic field strength distribution in the region. They estimated a range of B values from 800 to 26400 μG at both 450 and 850 µm. The strongest field strength is observed to be in the region between the BNKL object and the Southern part of OMC-1.

It is important to understand why there is such a large discrepancy between the results of Chuss et al. (2019) and Hwang et al. (2021) so that the study of the magnetic fields in OMC-1 can be utilized for further projects regarding molecular cloud collapse and star formation. This paper will analyze the investigations completed by these two groups to figure out if the means by which Hwang et al. (2021) and Chuss et al. (2019) calculated the angular dispersion component of the DCF method had a substantial effect on the magnetic field strength results. The analysis presented incorporates the results of the HAWC+ data obtained by Chuss et al. (2019) used in the angular dispersion calculation method from Hwang et al. (2021), combined with the velocity dispersion and volume density calculations from Chuss et al. (2019), to produce magnetic field strength values. Section 2 reviews the HAWC+/SOFIA observations used in this work. Section 3 describes the implementation of the 'unsharp masking' technique along with the calculation of the magnetic field strengths in each wavelength. A discussion of the results, implications, and future work are presented in Section 4. Lastly, final conclusions are described in Section 5.

2 Observations

Chuss et al. (2019) obtained photometry and polarimetry data of the OMC-1 region in December 2016 on Stratospheric Observatory for Infrared Astronomy (SOFIA) using the High-resolution Airborne Wideband Camera (HAWC+) (Harper et al., 2018) at wavelengths of 53, 89, 154, and 214 μm. They obtained additional polarimetry data in October-November 2017 and September 2018. The observing time per band ranged from 9 minutes for 53 μm to 2 minutes at 214 μm. Chuss et al. (2019) reduced the photometry data using CRUSH V2.4.2ALPHA1. Because of the relatively small fractional bandwidth of the filters, they made no color corrections to the data. They adopted a 15% calibration uncertainty for the 53, 89, and 154 μm bands and 20% for the 214 μm band based on the variance of HAWC+ measurements. The polarimetry data consists of maps of the Stokes I,

Q, and U parameters and their associated uncertainties for far-infrared (FIR) continuum emission. Polarized light is represented by these parameters where I is indicative of intensity and U and Q are indicative of polarization angle (Sto, 2021). The wavelengths of 53, 89, 154, and 214 μm were observed with nominal beam sizes of 4.9", 7.8", 13.6", and 18.2", respectively. They reduced the data using the V1.3.0-BETA3 (April 2018) version of the HAWC+ data reduction pipeline.

3 Methodology

3.1 Calculating Angular Dispersion

The methods used in calculating the angular dispersion of the HAWC+ data sets were based on Pattle et al. (2017) and Hwang et al. (2021), as described in Section 1.2. We first measured the mean polarization angle θ of the original Stokes Q and U maps to produce a map showing the mean polarization angle per pixel. This value is depicted through Equation (2).

$$\theta = 0.5 * \arctan \frac{U}{Q}. \tag{2}$$

We use 3×3, 5×5, and 7×7 pixel boxcar filters in the *convolve2d* function from Python's *SciPy* library to perform convolutions on the original Stokes U and Q maps. *convolve2d* moves the boxcar filter over the entire image to trace the large-scale magnetic field distribution. We then calculate the mean polarization angle $\bar{\theta}$ of the convoluted maps, as shown in Equation (3), where $\bar{U}$ and $\bar{Q}$ are the Stokes U and Q maps after convolutions have been performed. This is representative of the mean polarization angle of the large-scale magnetic field in OMC-1.

$$\bar{\theta} = 0.5 * \arctan \frac{\bar{U}}{\bar{Q}} \tag{3}$$

The mean polarization angle per pixel $\bar{\theta}$ of the large-scale field is then subtracted from the mean polarization angle per pixel θ of the total field map, resulting in a residual map, showing the deviation in angle of each pixel from the mean field direction $\delta\theta$, i.e. $\delta\theta_{i,j} = \theta_{i,j} - \bar{\theta}_{i,j}$ at pixel (i,j) Hwang et al. (2021).

Figure 2 shows the observed angular position map, Figure 3 shows the convoluted angular position map, and Figure 4 shows the residual angular position map created with the 3x3 kernel for the 214 μm data set, as examples. From the residual map, we can calculate σ_ϕ as the root-mean-squared of the angular differences throughout the map for each kernel size for each of the four wavelengths. Pattle et al. (2017) estimated the angular dispersion for the entirety of OMC-1. However, Hwang et al. (2021) suspected that each region within OMC-1 would have a distinct B and that a single total estimate of B for the region as a whole would not be an accurate representation, due to there being different magnetic turbulence in each region. Therefore, we incorporated object masks into this process to calculate the angular dispersion value in the BNKL object region, the Trapezium Cluster (HII), and the Orion Bar, as Hwang et al. (2021) did. When multiplied by the residual map, these object masks nullify all pixels not in the specified region, and we are able to calculate the root-mean-squared of each individual region. Table 1 lists σ_ϕ in degrees resulting from convolutions of each kernel size applied to each region in each of the four wavelengths. It is important to note that the values for σ_ϕ and B of the Orion Bar for the 154 mm and 214 mm wavelength bands are not present in any table in this paper. This is because they were excluded from analysis as they were heavily influenced by systematic errors in the polarization vectors.

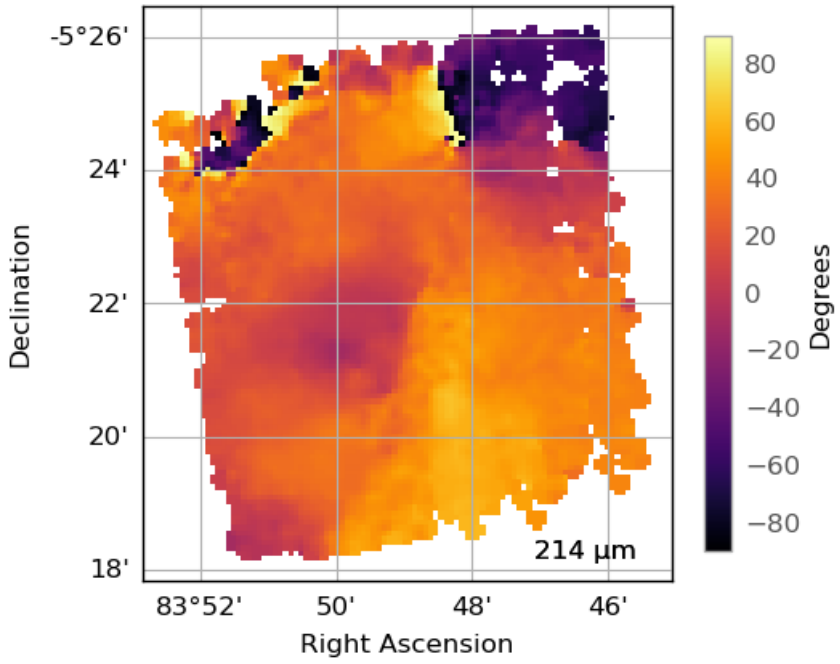

Figure 2: The observed angular position map produced by using Equation (2) on the Stokes U and Q maps. This is representative of the total polarization angle variations.

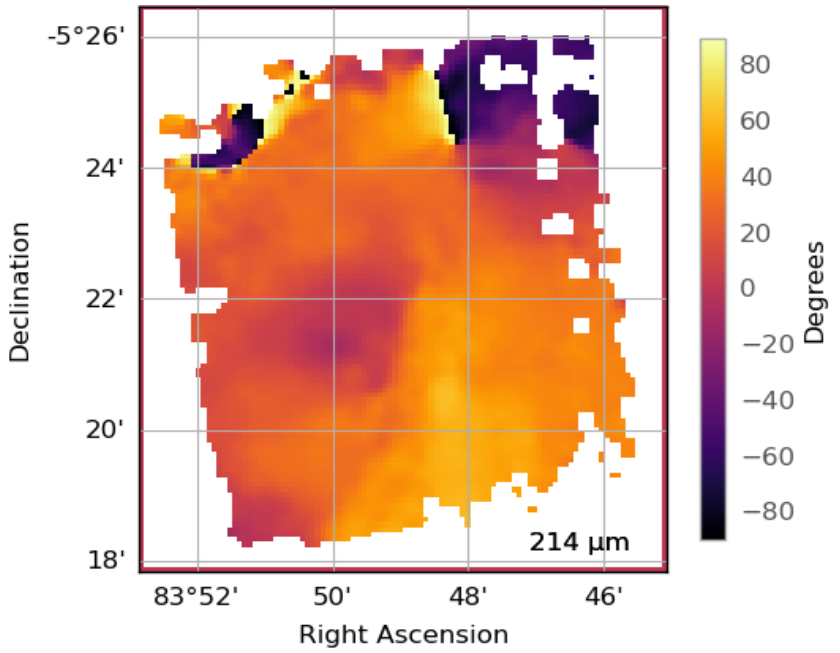

Figure 3: The convoluted angular position map produced using Equation (3) by applying convolutions with the 3x3 kernel size to the Stokes U and Q maps. This is representative of the large scale polarization angle variations.

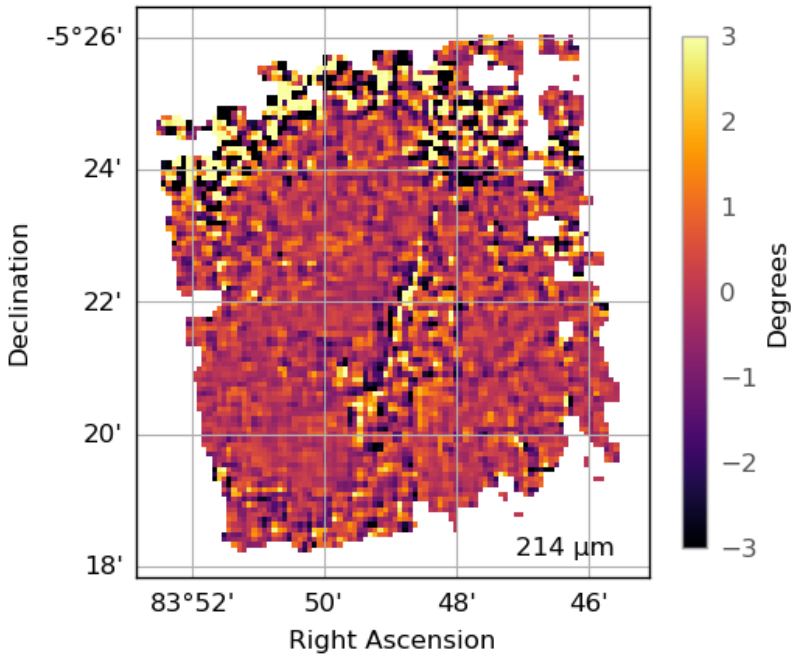

Figure 4: The resulting residual map by subtracting the convoluted map of Figure 3 from the observed map of Figure 2. This is representative of the small scale polarization angle variations.

Region	53 μm	89 μm	154 μm	214 μm
3x3 Kernel Size				
Bar	5.79	5.39	—	—
BNKL	2.34	1.90	2.80	2.72
HII	2.24	2.07	2.47	4.23
5x5 Kernel Size				
Bar	9.28	8.63	—	—
BNKL	3.63	2.96	4.82	3.75
HII	3.28	3.38	4.19	5.16
7x7 Kernel Size				
Bar	11.29	10.19	—	—
BNKL	4.41	4.04	5.94	4.79
HII	3.89	4.09	5.57	5.89

Table 1: The values of σ_ϕ (degrees) representing the polarization angle dispersions for each region in each data set are shown. They were calculated using each different kernel size.

Region	53 μm	89 μm	154 μm	214 μm
$\frac{\langle B_t^2 \rangle}{\langle B_0^2 \rangle}$				
Bar	1.61	1.77	—	—
BNKL	.370	.430	.370	.420
HII	.330	.230	.240	.340
σ_ϕ				
Bar	1.27	1.33	—	—
BNKL	.608	.656	.608	.648
HII	.574	.480	.490	.583

Table 2: $\frac{\langle B_t^2 \rangle}{\langle B_0^2 \rangle}$ and the converted σ_ϕ from Chuss et al. (2019).

Region	53 μm	89 μm	154 μm	214 μm
3x3 Kernel Size				
Bar	128.05	120.78	—	—
BNKL	117.43	97.17	128.59	122.97
HII	118.27	124.60	133.68	151.56
5x5 Kernel Size				
Bar	151.84	146.58	—	—
BNKL	142.56	127.42	155.17	141.02
HII	140.36	150.21	158.10	159.40
7x7 Kernel Size				
Bar	159.55	153.84	—	—
BNKL	151.49	144.14	162.86	152.36
HII	148.60	157.99	167.67	163.97

Table 3: The percent difference between the σ_ϕ values calculated through this analysis and from Chuss et al. (2019).

It is important to note that when Chuss et al. (2019) completed their analysis of angular dispersion, the dispersion function yielded this result in terms of a turbulent-to-ordered magnetic energy ratio. This ratio compares the turbulent magnetic field, B_t^2, to the ordered magnetic field, B_0^2. Equation (4) gives the relationship between the angular dispersion σ_ϕ in degrees and the turbulent-to-ordered magnetic energy ratio $\frac{B_t^2}{B_0^2}$ (Chuss et al., 2019). Through this manner, it became possible to directly compare the results from this study to those from Chuss et al. (2019). Table 2 shows $\frac{\langle B_t^2 \rangle}{\langle B_0^2 \rangle}$ from Chuss et al. (2019) and the corresponding σ_ϕ values using the conversion in Equation (4). Table 3 shows the percent difference between σ_ϕ calculated in this analysis and σ_ϕ from Chuss et al. (2019).

$$\sigma_\phi^2 = \frac{\langle B_t^2 \rangle}{\langle B_0^2 \rangle} \tag{4}$$

3.2 Calculating Magnetic Field Strengths

Once σ_ϕ was calculated for each wavelength for each kernel size, then we could utilize the DCF method in order to calculate the magnetic field strength. Chuss et al. (2019) calculated a uniform σ_v

Region	53 μm	89 μm	154 μm	214 μm
3x3 Kernel Size				
Bar	4189.99	4504.96	—	—
BNKL	16560.8	20419.1	13835.1	14248.0
HII	4238.05	4584.57	3842.63	2239.12
5x5 Kernel Size				
Bar	2615.37	2811.64	—	—
BNKL	10674.9	13081.3	8035.68	10331.8
HII	2891.88	2806.15	2262.39	1835.79
7x7 Kernel Size				
Bar	2149.16	2379.96	—	—
BNKL	8786.60	9577.73	6516.63	8076.13
HII	2433.67	2315.84	1699.96	1608.71

Table 4: B (μG) calculated from the DCF method using σ_ϕ from this analysis, and σ_v and ρ from Chuss et al. (2019).

over the entire OMC-1 region as 1.85 km/s. To calculate ρ, they used the relationship in Equation (5), where $N(H_2)$ is the average column density of molecular hydrogen (cm^{-2}), L is the uniform cloud depth (cm) over the entire OMC-1 region, μ is the mean molecular weight as determined by Sadavoy et al. (2013), and m_H is the atomic mass of hydrogen.

$$\rho = \frac{N(H_2)}{L}\mu m_H \tag{5}$$

The L utilized in this study is the same as calculated by Pattle et al. (2017), 4.34×10^{17} cm. The measured column density varied based on region. For the BNKL object, the HII region, and the Orion Bar, Chuss et al. (2019) measured the column densities to be $(9.85 \pm 8.96) \times 10^{22}$ cm^{-2}, $(3.87 \pm 2.21) \times 10^{22}$ cm^{-2}, and $(5.90 \pm 3.24) \times 10^{21}$ cm^{-2}, respectively. Table 4 shows the final results of the magnetic field strength values per region in each wavelength for each kernel size.

Something we must consider in this analysis is the signal integration in calculations of the turbulent-to-ordered magnetic energy ratio and B, as Houde et al. (2009) did in developing the DCF method. To do this, we must utilize the number of turbulent cells contained in the column of dust probed with our measurements, N (Houde et al., 2009). N shows what the effect of signal integration is through the thickness of the cloud and in the area covered by the telescope beam on the measured angular dispersion, and consequently the turbulent-to-ordered magnetic energy ratio (Houde et al., 2009). Upon Chuss et al. (2019)'s calculations of the turbulent-to-ordered magnetic ratio and B through the DCF method, N was already taken into account. However, the analysis of σ_ϕ and B completed in this paper did not take into account N. To correct for this, we multiplied the B values calculated by Chuss et al. (2019) by $\sqrt{N}$. See Section 3 of Houde et al. (2009) for a more detailed, mathematical discussion of the role of the $\sqrt{N}$ component in the calculation of the turbulent-to-ordered magnetic energy ratio and B. Table 5 depicts the original B values from Chuss et al. (2019), the N values from Chuss et al. (2019), as well as the product of B and $\sqrt{N}$, per region for each data set. Table 6 depicts the percent differences between B calculated from this study and the adjusted B calculated in Chuss et al. (2019).

	53 μm	89 μm	154 μm	214 μm
Original B (μG) from Chuss et al. (2019)				
Bar	303	289	—	—
BNKL	1002	931	1013	944
HII	261	316	305	259
N from Chuss et al. (2019)				
Bar	8.50	8.44	—	—
BNKL	6.67	8.42	5.02	4.02
HII	24.59	9.79	19.32	30.23
B (μG) $\times \sqrt{N}$				
Bar	883.39	839.594	—	—
BNKL	2587.8	2701.5	2269.67	1892.71
HII	1294.12	988.372	1340.61	1424.03

Table 5: The top row consists of the original B values in μm that Chuss et al. (2019) calculated. The middle row consists of the N values which correct for the signal integration factor. The lower row consists of the original B values from Chuss et al. (2019) multiplied by $\sqrt{N}$.

Region	53 μm	89 μm	154 μm	214 μm
3x3 Kernel Size				
Bar	130.35	137.16	—	—
BNKL	145.94	153.26	143.63	153.09
HII	106.43	129.06	96.54	44.50
5x5 Kernel Size				
Bar	99.01	108.02	—	—
BNKL	121.95	131.53	111.90	138.07
HII	76.34	95.81	51.17	25.26
7x7 Kernel Size				
Bar	83.48	95.69	—	—
BNKL	109.00	112.00	96.67	124.05
HII	61.14	80.35	23.64	12.18

Table 6: The percent difference between B (μG) calculated through this analysis and B (μG) calculated in Chuss et al. (2019), with the corrections described in Table 5.

4 Discussion

Upon calculating the percent differences between the angular dispersion and magnetic field strength results, it becomes apparent that there is a substantial difference between the results determined utilizing the 'unsharp masking' method and the dispersion function. This is indicative of the fact that the method used to calculate the angular dispersion component of the DCF method has an effect on the resulting magnetic field strength results. Therefore, this is likely a reason for why the B values from Chuss et al. (2019) and Hwang et al. (2021) vary by nearly an order-of-magnitude. B in both cases, however, is strong enough to affect the star formation process in OMC-1, so there must be a well-established method of how to calculate the angular dispersion in the DCF method.

4.1 Future Work

The first steps for the future are to determine the correct kernel size. Because each angular dispersion value produced in this analysis is different from those in Chuss et al. (2019), for the purposes of this analysis, the conclusion formed did not require an immediate assessment of which kernel size yielded the most accurate results. Following this, we can complete another study to use the SCUBA-2 data from Hwang et al. (2021) in the dispersion function which Chuss et al. (2019) used in their angular dispersion calculation. We can then utilize the DCF method with the velocity dispersion and volume density values calculated by Hwang et al. (2021) to determine what the magnetic field strength would be, similarly to what was done in this analysis. This would allow for us to determine how significant of an effect the dispersion function has on the magnetic field strength values calculated using the SCUBA-2 data, as opposed to the 'unsharp masking' technique. In order to determine which method produces more accurate results, we can create magneto-hydrodynamic simulations to calculate the magnetic field using the DCF method and other star formation analyses. We can compare the results from these simulations with what was done in this study and what will be done in subsequent ones to determine the drawbacks of each method. Additionally, it is clear from this study that the methods used to calculate angular dispersion contribute to the difference in magnetic field strength results, but we must also assess whether or not the methods used to calculate velocity dispersion and volume density components have a substantial impact. Once we know more regarding the impact that each variable in the DCF equation has on the resulting magnetic field strength, then we will be able to draw more thorough conclusions about where the discrepancies lie which cause the results from Chuss et al. (2019) and Hwang et al. (2021) to vary to the degree that they do.

5 Conclusions

The purpose of completing this analysis was to figure out if the means by which Hwang et al. (2021) and Chuss et al. (2019) calculated the angular dispersion σ_ϕ made a contribution to the roughly order-of-magnitude difference between their B results for the OMC-1 region. This was completed through reproducing the 'unsharp masking' technique, which Hwang et al. (2021) utilized as their σ_ϕ calculation method, on the HAWC+ data obtained by Chuss et al. (2019). This σ_ϕ result was used in the DCF method with the corresponding velocity dispersion and volume density calculations from Chuss et al. (2019). By keeping the data, velocity dispersion, and volume density factors the same but only changing the σ_ϕ calculation method, we were able to gauge how big of an effect this method had on the resulting B values.

The 'unsharp masking' method developed by Pattle et al. (2017) first involved forming the mean polarization angle map from the original Stokes Q and U maps, which showed the total position angle distribution over OMC-1. Then, we performed convolutions on the original Stokes Q and U maps by moving a small boxcar kernel of sizes 3×3, 5×5, and 7×7 centered at each pixel over the entirety of the maps. The mean polarization angle of the convoluted Stokes Q and U maps was then calculated for each pixel and a map was created depicting the position angles of the smoothed, large-scale magnetic field component. In order to gauge the position angles of the turbulent, small scale component, the mean polarization angle map of the large-scale component was subtracted from the total mean polarization angle map. Object masks were applied to this residual map to separate the regions of the BNKL object, HII region, and the Orion Bar. To determine what σ_ϕ was, we took the root-mean-squared of the residual map. This process was completed using each of the kernel sizes for each of the four wavelengths in which the data was obtained. Following this, using the velocity dispersion and volume density values obtained by Chuss et al. (2019), we calculated the magnetic field strength values.

To compare σ_ϕ values from this study to those from Chuss et al. (2019), we converted the turbulent-to-ordered magnetic energy ratio, which was provided in the literature, to σ_ϕ. We calculated the percent differences between the σ_ϕ values calculated in this study and those from Chuss et al. (2019). To compare magnetic field strength values, we adjusted those which were calculated by Chuss et al. (2019) by correcting for the signal integration factor, as described in Houde et al. (2009). We calculated the percent differences between the magnetic field strength values calculated in this study and those from Chuss et al. (2019) corrected for signal integration. These results allowed us to conclude that the methodologies used by Chuss et al. (2019) and Hwang et al. (2021) to calculate the angular dispersion of the magnetic field in OMC-1 did in fact play a substantial role in accounting for the roughly order-of-magnitude difference in magnetic field calculations between the two groups. The main components of future work involve extending this analysis by creating magneto-hydrodynamic simulations, incorporating the SCUBA-2 data in the dispersion function method to once again calculate the magnetic field strength, and analyzing the methods of the velocity dispersion and volume density calculations in each study. By doing this, we will be able to draw more precise conclusions about the accuracy of each angular dispersion calculation method, and work towards determining the primary reason for why the two published magnetic field strength values are different.

6 Acknowledgements

The author of this paper would like to acknowledge Jordan Guerra and David Chuss of the Villanova University Physics Department for acting as mentors throughout the duration of this research project. The author would also like to thank Joseph Michail and Catherine Petretti for help with the code. Finally, the author would like to acknowledge the professor of the class, Andrej Prsa, for teaching about the process, from beginning to end, of completing a research project in academia.

References

2021, Polarized Light and the Stokes Parameters, University of Victoria

Becklin, E. E., & Neugebauer, G. 1967, Apj, 147, 799

Chandrasekhar, S., & Fermi, E. 1953, apj, 118, 113. https://ui.adsabs.harvard.edu/abs/1953ApJ...118..113C

Chuss, D. T., Andersson, B. G., Bally, J., et al. 2019, Apj, 872, 187. https://arxiv.org/abs/1810.08233https://arxiv.org/abs/1810.08233

Friberg, P., Bastien, P., Berry, D., et al. 2016, in Millimeter, Submillimeter, and Far-Infrared Detectors and Instrumentation for Astronomy VIII, ed. W. S. Holland & J. Zmuidzinas, Vol. 9914, International Society for Optics and Photonics (SPIE), 1 – 9, doi: http://doi.org/10.1117/12.223194310.1117/12.2231943

Friesen, R. K., Pineda, J. E., co-PIs, et al. 2017, Apj, 843, 63. https://arxiv.org/abs/1704.06318https://arxiv.org/abs/1704.06318

Guerra, J. A., Chuss, D. T., Dowell, C. D., et al. 2021, The Astrophysical Journal, 908, 98. http://dx.doi.org/10.3847/1538-4357/abd6f0

Harper, D. A., Runyan, M. C., Dowell, C. D., et al. 2018, Journal of Astronomical Instrumentation, 07, 1840008, doi: http://doi.org/10.1142/S225117171840008110.1142/S2251171718400081

Heitsch, F. 2005, in Astronomical Society of the Pacific Conference Series, Vol. 343, Astronomical Polarimetry: Current Status and Future Directions, ed. A. Adamson, C. Aspin, C. Davis, & T. Fujiyoshi, 166

Hildebrand, R. H., Kirby, L., Dotson, J. L., Houde, M., & Vaillancourt, J. E. 2009, The Astrophysical Journal, 696, 567–573. http://dx.doi.org/10.1088/0004-637X/696/1/567

Houde, M., Dowell, C. D., Hildebrand, R. H., et al. 2004, The Astrophysical Journal, 604, 717

Houde, M., Vaillancourt, J. E., Hildebrand, R. H., Chitsazzadeh, S., & Kirby, L. 2009, Apj, 706, 1504. https://arxiv.org/abs/0909.5227https://arxiv.org/abs/0909.5227

Hwang, J., Kim, J., Pattle, K., et al. 2021, The Astrophysical Journal, 913, 85. http://dx.doi.org/10.3847/1538-4357/abf3c4

Kleinmann, D. E., & Low, F. J. 1967, Apj, 149, L1

Kounkel, M., Hartmann, L., Loinard, L., et al. 2017, The Astrophysical Journal, 834, 142. https://doi.org/10.3847/1538-4357/834/2/142

Lazarian, A., & Hoang, T. 2007, Monthly Notices of the Royal Astronomical Society, 378, 910

Pattle, K., Ward-Thompson, D., Berry, D., et al. 2017, The Astrophysical Journal, 846, 122. http://dx.doi.org/10.3847/1538-4357/aa80e5

Sadavoy, S. I., Francesco, J. D., Johnstone, D., et al. 2013, The Astrophysical Journal, 767, 126, doi: http://doi.org/10.1088/0004-637x/767/2/12610.1088/0004-637x/767/2/126

Schekochihin, A. A., & Cowley, S. C. 2007, Turbulence and Magnetic Fields in Astrophysical Plasmas (Dordrecht: Springer Netherlands), 85–115, doi: http://doi.org/10.1007/978-1-4020-4833-$3_6$10.1007/$978 - 1 - 4020 - 4833 - 3_6$

Schleuning, D. A. 1998, The Astrophysical Journal, 493, 811

Vallee, J. P., & Bastien, P. 1999, The Astrophysical Journal, 526, 819

Ward-Thompson, D., Pattle, K., Bastien, P., et al. 2017, The Astrophysical Journal, 842, 66